ELSEVIER

NeuroImage

www.elsevier.com/locate/ynimg
NeuroImage 23 (2004) S139–S150

# Geodesic estimation for large deformation anatomical shape averaging and interpolation

Brian Avants and James C. Gee*

*University of Pennsylvania, Philadelphia, PA 19104, United States*

Available online 11 September 2004

**The goal of this research is to promote variational methods for anatomical averaging that operate within the space of the underlying image registration problem. This approach is effective when using the large deformation viscous framework, where linear averaging is not valid, or in the elastic case. The theory behind this novel atlas building algorithm is similar to the traditional pairwise registration problem, but with single image forces replaced by average forces. These group forces drive an average transport ordinary differential equation allowing one to estimate the geodesic that moves an image toward the mean shape configuration. This model gives large deformation atlases that are optimal with respect to the shape manifold as defined by the data and the image registration assumptions. We use the techniques in the large deformation context here, but they also pertain to small deformation atlas construction. Furthermore, a natural, inherently inverse consistent image registration is gained for free, as is a tool for constant arc length geodesic shape interpolation. The geodesic atlas creation algorithm is quantitatively compared to the Euclidean anatomical average to elucidate the need for optimized atlases. The procedures generate improved average representations of highly variable anatomy from distinct populations.**


*Keywords:* Atlas creation; Nonrigid image registration; Inverse consistent; Geodesic averaging; Morphometry

## Introduction

Anatomical atlases have tremendous value in today's medical environment where large databases are mined for diagnostic, research, and pedagogical information. High-resolution atlases are an instance of anatomy upon which teaching or surgical planning is based (Kikinis et al., 1996; Miller et al., 1993; Yelnik et al., 2003). Surgical procedures may employ atlas-based image registration for planning the placement of deep-brain stimulators (Dawant et al., 2003). Average anatomical atlases provide a least-biased coordinate system for surgical planning, functional localization studies (Ashburner and Friston, 1996), or for studying structure–function relationships (Letovsky et al., 1998). They also operate as a reference frame for understanding the normal variation of anatomy (Talairach and Tournoux, 1988) and as a probabilistic space into which functional or structural features are mapped (Le Briquer and Gee, 1997). Genomics researchers currently build atlases to investigate the relationship of genotype to phenotype (Mackenzie-Graham et al., 2004), which is a major focus of the Allen Brain Institute (Allen Brain Atlas). Performance of algorithms based on manipulating empirical information, such as active shape (Cootes et al., 1995), should also benefit from use of an average model.

Computerized atlases based on magnetic resonance (MR) images may compile either average shape (Le Briquer and Gee, 1997), average intensity, or both (Guimond et al., 2000) within a single image. The Euclidean shape space, shown in Fig. 1, is often assumed for these models leading to the use of linear averaging of the transformations and intensity to produce the atlases. Deviations from the mean shape or intensity may then be captured separately by statistical models such as principal components (Cootes et al., 1995; Le Briquer and Gee, 1997). Average intensities are traditionally found by first computing transformations from an anatomical instance to a population data set. The averages of these displacement fields, which take a member of the population to the remainder of the data, represent an average in the sense of anatomical positions. This average transformation must then be inverted to gain the average shape (Guimond et al., 2000). However, positional differences are not explicitly minimized in the registration problem, typically because one promotes smoothness by using differential measures in the face of ill-posed problems (Tikhonov and Arsenin, 1977).

One difficulty with this approach is that the process of averaging transformations may destroy the optimal properties of the individual transformations. For example, the average of large deformation displacement fields, each of which satisfies the minimization of a well-defined variational energy, may no longer

* Corresponding author. University of Pennsylvania, 3600 Market Street, Suite 370, Philadelphia, PA 19104. Fax: +1 619 349 8552.
*E-mail addresses:* avants@grasp.cis.upenn.edu (B. Avants), gee@grasp.cis.upenn.edu (J.C. Gee).
**Available online on ScienceDirect (www.sciencedirect.com.)**

1053-8119/$ - see front matter © 2004 Elsevier Inc. All rights reserved.
doi:10.1016/j.neuroimage.2004.07.010

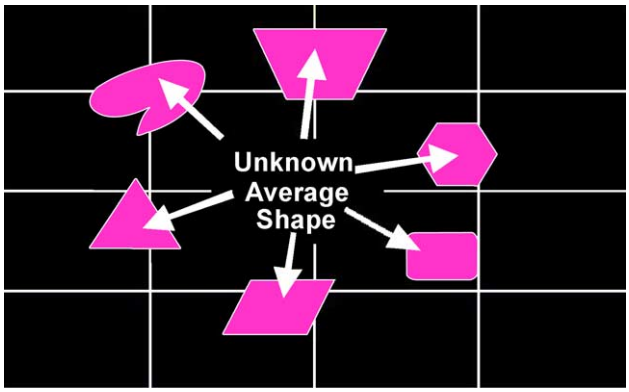


Fig. 1. The linear shape space.

be a legitimate displacement field with respect to the optimized quantities. Another example is found in time-parameterized mappings. The flows defining these transformations at each time satisfy the fluid equations, allowing the maps to be interpreted as members of the diffeomorphism group (Miller and Younes, 2001). Averaging the final displacements in these maps eliminates the optimality in space and time.

Optimization-based atlases respect the underlying manifold structure of the optimization problem (Yezzi and Soatto, 2003). Large deformation image registration is important for studying anatomical variation within groups and, more importantly, for the comparison of topologically dissimilar groups such as normal vs. highly atrophied brains, interspecies comparisons, as well as anatomical growth and development. One approach for comparing very distinct groups is to base comparison on their representative atlases. Large deformation atlases may be used to compactly represent a group and its shape or intensity variations.

The large deformation image registration framework invites group theoretical population studies where one bases structural comparisons on the geodesic distances between members of the group. Thus, it is important to be able to compute atlases that are least biased within this theoretical framework, as well as in the small deformation elastic case.

This work provides a flexible algorithm for allowing shape averaging that enables properties of the physical model used in the registration to persist in the average shape transformation. The distances from the diffeomorphism group are used to illustrate the techniques. Thus, geodesic averaging, rather than linear averaging, is used to estimate mean atlas shapes. We find the average representation of anatomy by using the same optimization framework as is assumed for the image registration itself. This kind of averaging is a metaregistration algorithm operating with average forces along the shape manifold. This explicit optimization inherently respects the optimization problem and implies a basic framework for large deformation statistics. Here we compute means, but variances and principal components that are optimal in time should follow. The framework allows either large or small deformation averaging and realizes different outcomes than simply taking the naive Euclidean mean of displacements.

## Methodology

The goal of this paper is to point out that average anatomical shape atlases should be computed with respect to the assumptions of the image registration problem. This simplifies the atlas estimation: the same algorithm used for pairwise registration should be the foundation of an algorithm for computing the transformation from an initial atlas to the optimal atlas. Given a variational registration algorithm $\mathcal{A}$ that solves the pairwise problem, one simply invokes a meta-algorithm $\bar{\mathcal{A}}$ that replaces an individual image and its forces with a data set of images and the average forces. We will follow this general philosophy using an extension of the group theoretical diffeomorphic registration algorithm as $\mathcal{A}$ (Miller and Younes, 2001).

### *Mathematical background*

The basic notion of computational anatomy is related to the theory of categories, in which one studies a collection of objects and the mappings between those objects. Neuroanatomical images defined on an open domain $\Omega$ and with an approximately consistent topology are an example of an object collection. In computational anatomy, the group of diffeomorphisms gives one-to-one mappings between the objects in the collection. The diffeomorphisms are $C^n$ smooth, invertible, topology preserving transformations. Thus, anatomy without "holes" remains without holes under the action of a diffeomorphism.

Consider a set of anatomical images defined on bounded domain $\Omega$, each of which contains identical topology initially at positions $\{x_i\}$. Shape normalization requires a reparameterization of this population data set, $P = \{x_i\}$ into a common coordinate space. Each coordinate $\bar{\mathbf{x}}$ then identifies the same anatomical position in each example. Formally, this requires a mapping set $\{\boldsymbol{g}_i: \bar{\mathbf{x}} \rightarrow \mathbf{x}_i\}$ such that,

$$\begin{aligned} \mathbf{g}_1^{-1}\mathbf{x}_1 &= \bar{\mathbf{x}} \\ &\cdots \\ \mathbf{g}_n^{-1}\mathbf{x}_n &= \bar{\mathbf{x}} \end{aligned} \tag{1}$$

Each mapping holds the coordinate transformation between the canonical configuration $\bar{\mathbf{x}}$ and $\mathbf{x_i}$, such that $\boldsymbol{g}_i = \mathbf{Id} + \mathbf{u}$, where $\mathbf{Id}$ is the identity. Th mean shape is $\boldsymbol{g}_i(\bar{\mathbf{x}}) = \bar{\mathbf{x}} + \mathbf{u}(\bar{\mathbf{x}}) = \mathbf{x_i}$. If $\boldsymbol{g}_i$ is time parameterized in interval [0, 1], its value is taken at $\boldsymbol{g}_i$ (1), the final state.

The individual mappings $\boldsymbol{g}_i$ may be found by using a variety of nonrigid image registration algorithms (Ashburner and Friston, 1996; Christensen et al., 1993; Le Briquer and Gee, 1997; Rueckert et al., 1999). These methods return a displacement field $\mathbf{u}$ that models the motion of a continuum deforming under external forces. Solutions of this kind minimize a balance of regularization and similarity terms. The displacement field is found in either the Lagrangian reference frame, where the reference configuration $\mathbf{x}$ is fixed, or in the Eulerian frame, where the configuration is a function of time $\mathbf{x}(t)$. Provided a value for $\mathbf{u}$, the solution will transform the moving image $J(\mathbf{x}_i)$ to the fixed domain $I(\bar{\mathbf{x}})$ such that $J'(\bar{\mathbf{x}}) = J(\mathbf{Id} + \mathbf{u}_i^{-1})(\mathbf{x}_i) = J \circ \boldsymbol{g}_i^{-1} \circ \mathbf{x_i}$. We will denote the images $I = I(\mathbf{x})$ and $J = J(\mathbf{y})$ with the spatial coordinates implied.

The transformation model for the nonrigid registration used here is the one-parameter diffeomorphism group $\mathcal{G}$. The group $\mathcal{G}$ transforms the underlying space $\Omega$ through a map $\phi$ with the following properties,

(1) $\phi(\mathbf{Id}, \Omega) = \Omega$ where $\mathbf{Id}$ is identity in $\mathcal{G}$ and
(2) $\phi(\boldsymbol{g}, \phi(\boldsymbol{h}, \Omega)) = \phi(\boldsymbol{g} \circ \boldsymbol{h}, \Omega), \forall \boldsymbol{g}, \boldsymbol{h} \in \mathcal{G}$.

These are known as right actions and may also be thought of as mappings or coordinate transformations on the objects. The use of composition in the definition of the map, $\phi$, delivers the group structure to $\mathcal{G}$, with $\phi$ the group action. Additionally, the group orbit is the set of objects that may be formed when one applies the group to an individual object $I$. Noting that $I\boldsymbol{g} = I \circ \boldsymbol{g} \circ \mathbf{x}$, the orbit of, for example, neuroanatomical image $I$ is then $\{I\boldsymbol{g}\}$, where there exists a separate orbit for anatomical image $J$, $\{J\boldsymbol{h}\}$ (Grenander and Miller, 1998).

*Flows for diffeomorphic image registration*

The transformation of anatomical images with respect to the diffeomorphism group is obtained by studying time dependent action $\boldsymbol{g}$ generated by velocity fields or flows $\boldsymbol{v}$ on $\Omega$. The mapping $\phi(t) = \boldsymbol{g}(t)(\boldsymbol{x})$ emerges from a transport ordinary differential equation,

$$\begin{cases} \frac{\mathrm{d}}{\mathrm{d}t}\boldsymbol{g}(t)(\boldsymbol{x}) & = \boldsymbol{v}(\boldsymbol{g}(t)(\boldsymbol{x})) \\ \boldsymbol{g}(0) & = \boldsymbol{g}_0. \end{cases} \tag{2}$$

Integrating the incremental solutions from time zero to time $t = 1$,

$$\boldsymbol{g}(1) = \int_{t=0}^{t=1} \boldsymbol{v}(\boldsymbol{g}(t))\mathrm{d}t, \tag{3}$$

imparts the final diffeomorphic map $\phi = \boldsymbol{g}$ (1) where $\phi$ is a solution of the transport o.d.e. in Eq. (2).

The group theoretical formulation allows one to measure distances between anatomical instances $I$ and $J$ with a true mathematical metric. The goal is then to find the shortest path between instances of the anatomy via the group action. The image registration and metric are gained through solving the variational problem below (Dupuis et al., 1998),

$$\text{Solve} : D(I,J) = \inf_{\boldsymbol{v}} \left\{ \int_0^1 \|\mathrm{L}\boldsymbol{v}\|\mathrm{d}t \right\}, \text{ with } I(\phi(\mathbf{x})) = J(\mathbf{y}). \tag{4}$$

The length $D$ is defined with respect to the linear operator $L$. Here, it is the Cauchy–Navier operator,

$$L = \mu\nabla^2 + (\lambda + \mu)\vec{\nabla}(\vec{\nabla}\cdot). \tag{5}$$

The differential norm $\|\cdot\|_L = \|L\cdot\|$ on $\boldsymbol{v}$ is determined by the associated linear operator $L$ where $\|\cdot\|$ is the standard $L^2$ norm defined for square integrable functions (and thus implying integration over the spatial variable). This is a true distance in that it is positive, symmetric, and satisfies the triangle inequality (Miller et al., 2002). The incremental integration of the velocity field is essential to this property (consider that the flow along the velocity field is, in the infinitesimial limit, piece-wise linear with equivalent norm forward and backward in time). In contrast, deformation-based norms taken from continuum mechanics are also positive and equal zero at the identity, but may not be symmetric.

Optimization of these energies issues the solution $\boldsymbol{g}^*$, mapping between $I$ and $J$. These definitions provide an appropriate notion of the curved geometric distance between two instances of anatomy. If one's velocity field is not smooth or the domain configurations ($I$, $J$) are not reachable from each other, then the updates to $\boldsymbol{g}$ will need to be infinitesimally small to maintain diffeomorphism and the endpoint condition will never be met, yielding an infinite distance. The Euler–Lagrange (E–L) equations for this problem were recently derived (Miller et al., 2002). Rather than using the local E–L equations, we solve the variational problem in the integral form by using the Galerkin finite element (FE) method (Zienkiewicz, 1971).

*Symmetric formulation for the velocity field*

The transformation $\phi$ is often applied only to image $I$. This introduces an inherent and undesirable asymmetry to the optimization process that has negative effects on both the registration performance and the symmetry of the metric computation. The asymmetry is reduced here by considering that,

$$(\boldsymbol{v}_{\boldsymbol{h}}(\boldsymbol{h}(1-t)))^{-1} = \boldsymbol{v}_{\boldsymbol{g}}(\boldsymbol{g}(t)). \tag{6}$$

Optimization with respect to $\boldsymbol{g}$ then directly implies optimization with respect to $\boldsymbol{h}$, where $\boldsymbol{h}$ is operating in the time-reversed direction of $\boldsymbol{g}$,

$$\boldsymbol{v}^* = \underset{\boldsymbol{v}}{\operatorname{argmin}} \left\{ \frac{1}{2} \int_0^1 \left( \|L\boldsymbol{v}\|^2 + \|I\boldsymbol{g}^{-1}(t)(\boldsymbol{x}) - J(\boldsymbol{x})\|^2 \right) \mathrm{d}t \right\}, \tag{7}$$

with $\boldsymbol{x} = \boldsymbol{h}^{-1}(1-t)(\boldsymbol{y})$.

Note that $\|I\boldsymbol{g}^{-1}(t)(\boldsymbol{x}) - J(\boldsymbol{x})\| = \|J\boldsymbol{h}^{-1}(1-t)(\boldsymbol{y}) - I(\boldsymbol{y})\|$. Recalling Eq. (6), minimization with respect to $\boldsymbol{v}$ yields $(I\boldsymbol{g}^{-1}(t)(\boldsymbol{x}) - J(\boldsymbol{x}))(\nabla I\boldsymbol{g}^{-1}(t)(\boldsymbol{x}) + \nabla J(\boldsymbol{x}))$, the optimal symmetric similarity gradient in the space of diffeomorphic flows. Regridding of the domain substitutes, here, for the jacobian term arising from a change of variables (thus, at any time, regridding sets $\boldsymbol{g}$ temporarily to **Id**, though the total $\boldsymbol{g}$ is saved). The main point here is that gradients with respect to both $I$ and $J$ come into play, thus giving a symmetry with respect to the image features guiding the registration. This locally symmetric computation is illustrated, along with the flow and its integration, in Fig. 2. Note that it is also possible to register the images by solving for $\boldsymbol{g}$ forward from time zero and backward from time 1 such that the images "meet" at time 0.5 in a mean configuration (Avants and Gee, 2004a, 2004b; Davis et al., 2004). This "inverse consistent" formulation requires both $\boldsymbol{h}$ and $\boldsymbol{g}$ to be stored and will be derived later in the text.

*Constant arc length constraint*

The optimal approximation to the time-integrated map requires parameterization of $\boldsymbol{g}$ by arc length, the unique and natural choice for (even infinite-dimensional) curves. The time-dependent integral for $\boldsymbol{g}$ is estimated with finite differences in time via the trapezoidal rule. Because the optimization process is not locally smooth in time, we measure the arc length at a step-size $h$ that is larger than that of the optimization step-size $\|\delta L\boldsymbol{v}\|$, with $\delta$ a small scalar. This is illustrated for a one-dimensional map in Fig. 3 (the ratio of step size $h$ to the optimization step size is typically near 0.1). The incremental velocities are accumulated via gradient descent such that $\mathbf{v}^*(t) \approx \mathbf{Id} + \sum_{i=0}^{i=n} \delta\mathbf{v}_i$. The total map $\boldsymbol{g}(t)$ is then integrated to $\boldsymbol{g}(t+h)$ using $\boldsymbol{v}^*(t)$ when

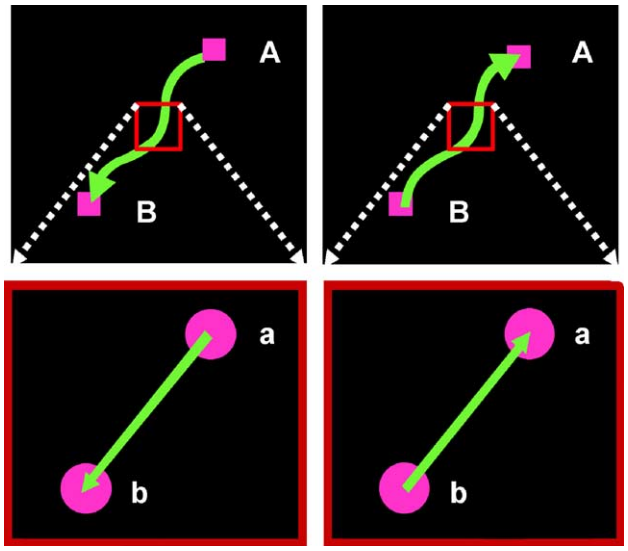


A symmetric flow is computed for each pairing of pixels, (A,B), by considering the image forces operating in each direction at the local scale. Solving forward or backward along the same path will then use the same image features (gradients).

Fig. 2. The computation of the optimal $\boldsymbol{v}$ uses gradients from both images.

$\|L\boldsymbol{v}^*(t)\|$ reaches the desired constant value $h$. If the arc length oversteps $h$, a local line search on $\delta\boldsymbol{v}_n$ corrects the size of $\|L\boldsymbol{v}^*\|$. The trapezoidal rule then provides the optimal in time approximation to the length as,

$$\int_{t_a}^{t_b} \|v(t)\|_L \mathrm{d}t \approx \sum_{i=1}^{i=n} \frac{h}{2}\left(\|\boldsymbol{v}(t_i + (i-1)h)\|_L + \|\boldsymbol{v}(t_i + ih)\|_L\right). \tag{8}$$

This approach contributes a more robust estimate of the geodesic distance and is also beneficial for the shape averaging application (we have found the distances estimated by the greedy algorithm in Christensen et al., 1993 are too noisy). To summarize, the following steps are needed in the algorithm for computing geodesics:

(1) Solve for the instantaneous regularized velocity field.
(2) Use the locally optimal solution above in a second gradient descent step, accumulating $\delta\boldsymbol{v}$ until the arc length reaches $h$.
(3) Integrate $\boldsymbol{v}$ to augment $\boldsymbol{g}$ in time and to compute a robust estimate of the geodesic distance.

Note the advantage that the velocity field is only needed at two time points, although an optimal in time solution is computed. Regridding may also be performed, as in Christensen et al. (1993).

*Robust intensity constraint*

An additional modification to the traditional viscous framework is the introduction of a robust similarity potential such that $\|I - J\|$ is replaced by robust function $\rho(I - J)$. A similar idea was used in Gee and Haynor (1996) and Hellier et al. (2001). Here, the metric is linear beyond robustness parameter gamma, such that,

$$\begin{cases} \text{if } x < \gamma \text{ then } \rho(x) = x^2, \\ \text{else if } x \geq \gamma \text{ then } \rho(x) = \gamma + |x - y|. \end{cases}$$

In our applications, $\gamma$ is set to 0.01 when the image histograms are matched and normalized to the interval [0, 1]. The robust function is shown in Fig. 4, while its improved performance is in Fig. 5. Similarly, an intensity-based evaluation of this registration algorithm's optimization capabilities is summarized in Fig. 6.

## Population shape averaging algorithms

The image registration algorithm described in the previous section allows the computation of transformations between the domains in a population data set. The traditional linear averaging for atlas estimation will be discussed first, followed by the novel geodesic averaging method. Examples will illustrate the need for the geodesic optimization algorithm.

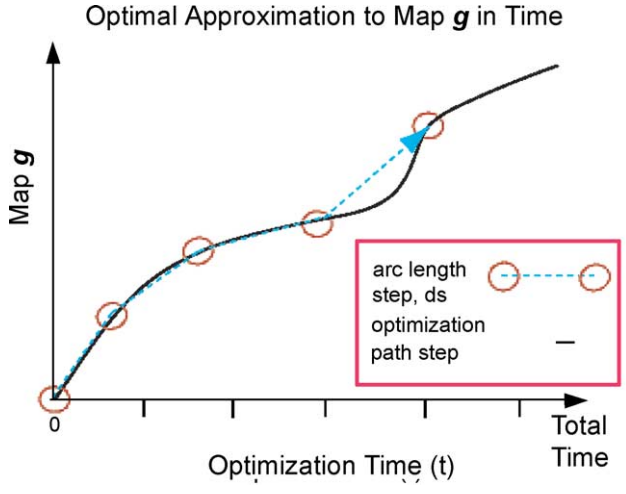


Fig. 3. The computation of the optimal $\boldsymbol{g}$ in time is performed using the trapezoidal rule, requiring constant arc length parameterization.

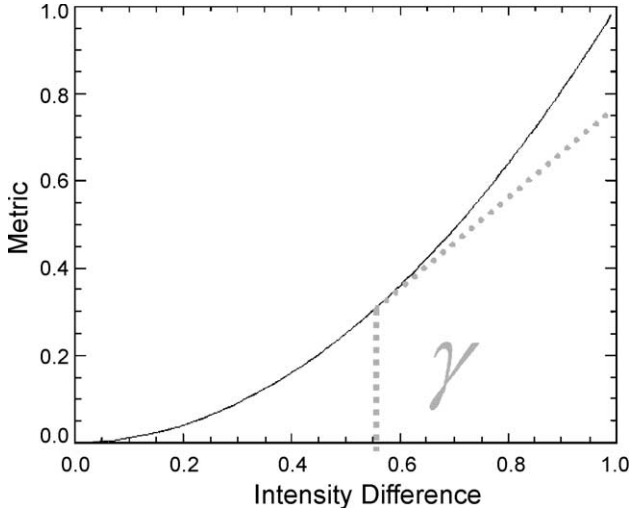


Fig. 4. The robust potential is used (dashed line) rather than the parabolic potential (solid line).

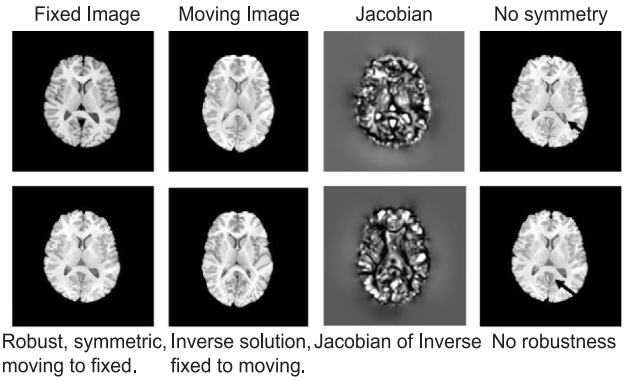


Fig. 5. The robust potential with symmetric velocity field is used to register the "fixed" and "moving" image. Note that the jacobians (right of center) are smooth and that forward and inverse direction are reflective of the expected shape changes (e.g., in the ventricles). The right column shows the benefit of the symmetric flow (top right, arrow, where one can see some nonventricular tissue being deformed into the ventricles) and the robust potential (bottom right, arrow, where one can see that the "hole" in the "fixed" image causes a large error in the registration that is not present in the robust case).

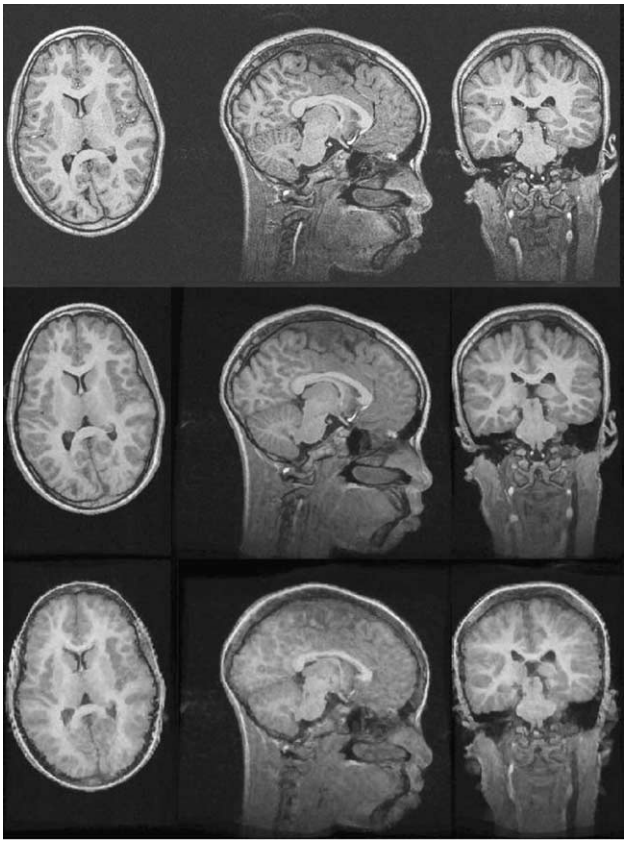

Fig. 6. A data set of 12 whole head MR images was registered to an arbitrary atlas (top row) with the ITK 1.6 Demons algorithm (bottom row) and with the viscous flow with the robust symmetric similarity here (middle row). The registered image intensities were then averaged linearly. The viscous flow produces a crisper average image than the ITK 1.6 Demons algorithm. Note that this is an evaluation that only investigates the intensity optimization and does not use anatomical information explicitly.

*Shape average from mean deformation: linear averaging*

We assume an underlying linear shape space, as in Fig. 1, and that a registration algorithm provides correspondence fields. Given the ability to compute this solution, average shapes are found by choosing an arbitrary instance as the reference configuration $\mathbf{x_o} = \mathbf{x_j}$ and then computing $\{\boldsymbol{g}_i\}$ with respect to this configuration. The average displacement field from $\mathbf{x_o}$ to $\{\mathbf{x}_i\}$ is,

$$\bar{\mathbf{u}}(\mathbf{x_o}) = (N)^{-1} \sum_{i=1}^{N} \mathbf{u}_i. \tag{9}$$

This mean deformation minimizes the energy,

$$\bar{\mathbf{u}}(\mathbf{x_o}) = \underset{\mathbf{u}}{\operatorname{argmin}} \frac{1}{2} \sum_{i=1}^{N} |\mathbf{u}_i - \mathbf{u}|^2. \tag{10}$$

Note that, as the total displacement fields are used, all scales of information are treated equally. The average configuration is then computed as $\bar{\mathbf{x}} = \bar{\mathbf{g}}^{-1}\ \mathbf{x_o}$, where an inversion of the mean deformation field is required (see Appendix for one approach). Averaging of vector fields does not necessarily preserve the large deformation continuum model, nor does it satisfy the correct optimization model, as illustrated in Figs. 7 and 8.

## Curved case: averaging with the diffeomorphism group

The algorithm $\mathcal{A}$ will now be extended into algorithm $\bar{\mathcal{A}}$ for an optimized estimate of the large deformation atlas.

*The variational problem for diffeomorphic averaging*

As seen in Fig. 8, the manifold shape is determined by the transformation model as well as the similarity criterion (intensity relationships, landmarks, etc.) and is illustrated in Fig. 9. Although the global surface is curved, each point on the manifold looks locally Euclidean in its tangent space. This fact will be exploited to compute

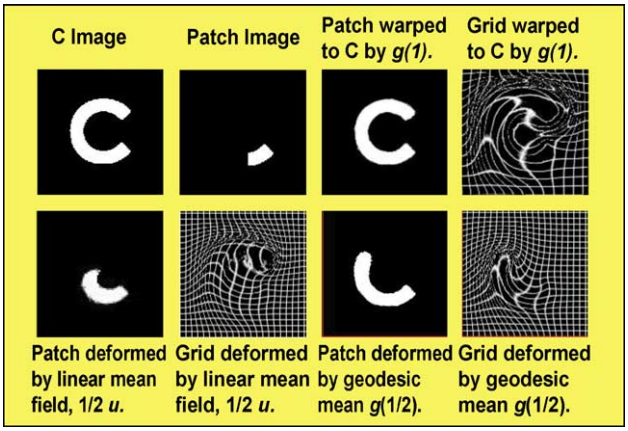


Fig. 7. The "C" and "C patch" images (first and second in the top row) are registered with the large deformation diffeomorphic method in the top row, giving transformation $\boldsymbol{g}(t)$. The linear average of the vector field $\mathbf{u}$ at $\boldsymbol{g}(1)$ with $\mathbf{Id}$ is shown in the bottom row left and left middle. The averaging with geodesic distances, at bottom row right, is more natural. Deformed grid images are also shown for the geodesic average. The jacobian of the C to C patch map is strictly positive with minimum value 0.14.

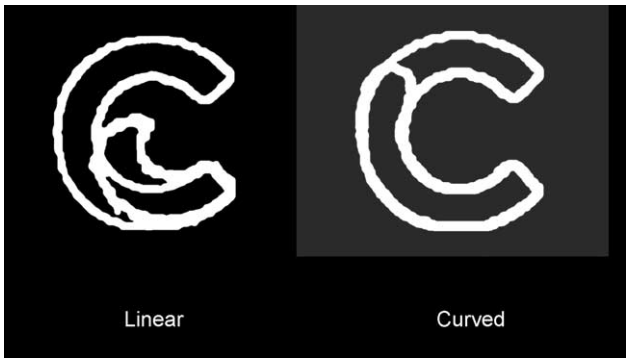


Fig. 8. The edge maps of the linear (left) and geodesic (right) "C" and "C patch" average shapes are overlayed on the edge map of the "C" image. The Euclidean average decouples the averaging from the registration problem and does not satisfy the optimization constraints that are inherent to the problem.

means of local velocity fields and to solve a mean transport ordinary differential equation that engenders a mean flow. This allows us to estimate optimal geodesic paths with respect to the manifold and permits registration of the whole database at once.

We recover the average-shape image from an image data set by solving an inverse problem involving the geodesic distances between the images and a boundary value constraint on the transformed image appearances. Find $\{g_i\}$ such that,

$$\begin{cases} \forall j \; I_j \circ \boldsymbol{g}_j^{-1} = I_j \boldsymbol{g}_j^{-1} = & \bar{I} \\ E\left(\left\{\boldsymbol{g}_j\right\}\right) & \text{is minimal.} \end{cases} \tag{11}$$

The distance $E$ in this case is the sum over the shape database of distances defined in Eq. (4). The existence of geodesic paths on the diffeomorphism manifold and the symmetry of those paths' distances are important facts for this algorithm. Furthermore, these paths, as mentioned above for the pairwise case, are also parameterized with constant arc length. Convexity is not guaranteed, here, as the problem is fundamentally ill posed. This is in contrast to the work by Fletcher et al. (2003) in which the optimization problem does not have a data term.

The simplest nontrivial case of this inverse problem is a single pair of images. First, regard the naive algorithm for minimization.

(1) Register images $I$ and $J$ while measuring the distance $D$ ($I$, $J$)($t$), between them.
(2) Repeat the registration stopping at $t_{(1/2)}$, where $D(I, J)(t_{(1/2)}) = (1/2)\, D(I, J)(t = 1)$.

This numerical minimization can be achieved successfully and was used in Fig. 7. However, the practical optimization process continues in a coarse to fine fashion causing coarse scale corrections to occur first in time. This is an undesirable bias that makes the averages appear visually incorrect when features exist at multiple scales, such as in anatomical images.

The key to finding the correct velocities is to solve a variational problem derived from Eq. (11) explicitly. First we give the average version of the transport ordinary differential equation,

$$\begin{cases} \frac{\mathrm{d}}{\mathrm{d}t}\bar{\boldsymbol{g}}\;(t)(\boldsymbol{x}) & = \bar{\boldsymbol{v}}\;(\bar{\boldsymbol{g}}(t)(\boldsymbol{x})), \\ \bar{\boldsymbol{g}}\;(0) & = \bar{\boldsymbol{g}}_0. \end{cases} \tag{12}$$

The initial value $\boldsymbol{g}_0$ is again the identity **Id**. Integrating the incremental solutions from time zero to time $t = 1$ will now result in the average diffeomorphic transformation,

$$\bar{\boldsymbol{g}}(1) = \int_{t=0}^{t=1} \bar{\boldsymbol{v}}(\bar{\boldsymbol{g}}(t))\mathrm{d}t, \tag{13}$$

which in turn holds forth the final diffeomorphic map $\bar{\phi} = \bar{\mathrm{g}}\,(1)$. First, consider the case of two images. The variational problem is then,

$$\boldsymbol{g}_1{}^*, \boldsymbol{g}_2{}^* = \underset{\boldsymbol{v}_1(t)}{\operatorname{argmin}} \underset{\boldsymbol{v}_2(t)}{\operatorname{argmin}} \left\{ \int_0^1 \|\boldsymbol{v}_1\|_L^2 + \|\boldsymbol{v}_2\|_L^2 + \|\mathrm{I}\boldsymbol{g}_1^{-1} - \bar{I}\|\mathrm{d}t \right\}$$
$$+ \|\mathrm{J}\boldsymbol{g}_2^{-1} - \bar{I}\|\mathrm{d}t.$$

We then rearrange terms using the equality constraints from the original problem statement,

$$\boldsymbol{g}_1{}^*, \boldsymbol{g}_2{}^* = \underset{\boldsymbol{v}_1(t)}{\operatorname{argmin}} \underset{\boldsymbol{v}_2(t)}{\operatorname{argmin}} \left\{ \int_0^1 \|\boldsymbol{v}_1\|_L^2 + \|\boldsymbol{v}_2\|_L^2 \right.$$
$$\left. + \|\mathrm{I}\boldsymbol{g}_1^{-1} - \mathrm{I}\boldsymbol{g}_2^{-1}\|\mathrm{d}t \right\}. \tag{14}$$

Solving via alternating minimization with respect to $\boldsymbol{g}_i$, and all $h_i$ constant, provides average deformations that are optimized symmetrically using information at all scales. The geodesic averaging constraint $E(\boldsymbol{g}_1) = E(\boldsymbol{g}_2)$ is upheld by construction and the configurations $I\boldsymbol{g}_1^{-1}$ and $J\boldsymbol{g}_2^{-1}$ are both in average position. Note also that this inverse consistent transformation from $I$ to $J$ is $\boldsymbol{g}_1^{-1} \circ \boldsymbol{g}_2$ (Fig. 10). This is distinct from the ideas of Johnson and Christensen (2001) in which a variational term is used to estimate consistency, as the inverse consistency here is inherent to the theory. We will denote the output of this algorithm as $\bar{\mathcal{A}}_2(\cdot,\cdot)$ where the input is a pair of images. Intuitively, the algorithm lets the images $I$ and $J$ "meet" at the mean configuration. An illustration of this approach for geodesic shape interpolation is shown in Fig. 11.

The algorithm for Eq. (12) when averaging a large database will be denoted $\bar{\mathcal{A}}$ ($\bar{\mathrm{I}}$, $\{I_1, \cdots, I_N\}$). This solves for the average transport differential equation $\dot{\bar{\boldsymbol{g}}} = \bar{\boldsymbol{v}}(\bar{\boldsymbol{g}})$, with $\bar{\boldsymbol{g}}(0) = \boldsymbol{x}$. The bar in $\bar{\mathrm{g}}$ denotes a mean value taken over the data set with $\bar{\boldsymbol{v}} = (1/N)\sum_i \boldsymbol{v}_i$ and the dot in $\dot{\boldsymbol{g}}$ indicating a time derivative. This requires solution of a

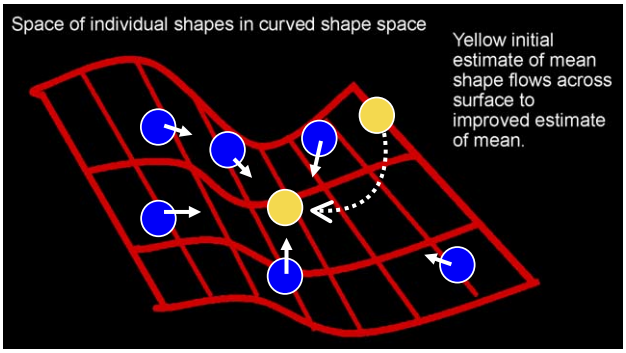


Fig. 9. The curved shape space and an illustration of a mean geodesic flow toward an optimal position on the manifold (with respect to the other shapes). Note that the average shape flows as do the members of the database.

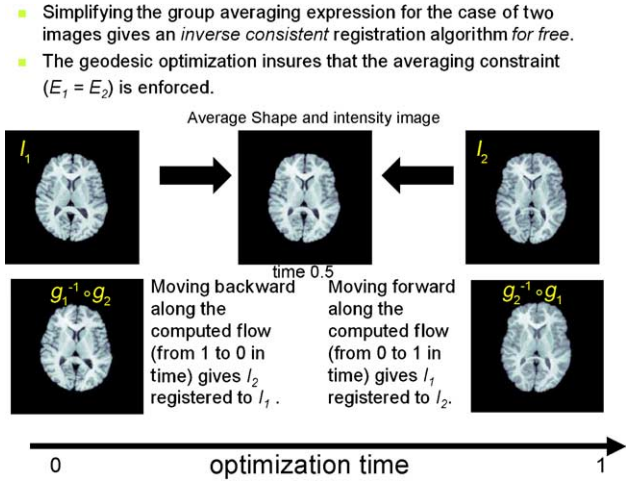


Fig. 10. The inverse consistent registration of two images is shown.

variational problem for $\boldsymbol{v}^*$ where the full database is used. This algorithm is summarized as,

(1) For each time, $t$, initializes $\bar{\boldsymbol{v}} = \mathbf{Id}$.

(2) For time $t$, use the constant arc length estimation method to solve the following problem for each $i \in \{1,\ldots,N\}$,

$$\boldsymbol{v}_1{}^* = \underset{\boldsymbol{v}_1(t)}{\operatorname{argmin}} \left\{ \|\boldsymbol{v}_i\|_L^2 + c\|I_i\bar{\boldsymbol{g}}^{-1} - \bar{I}\boldsymbol{g}^{-1}\| \right\}, \tag{15}$$

noting that symmetric flows are computed with respect to the domain of $\bar{\mathrm{I}}$.

(3) Set optimal $\bar{\boldsymbol{v}}^*(\boldsymbol{x}) = (1/N)\ \sum_i \boldsymbol{v}_i{}^*(\boldsymbol{x})$ and also $\|\bar{\boldsymbol{v}}(\boldsymbol{x})\|_L = h$. This is achieved in the same way as in the constant arc length constraint section.

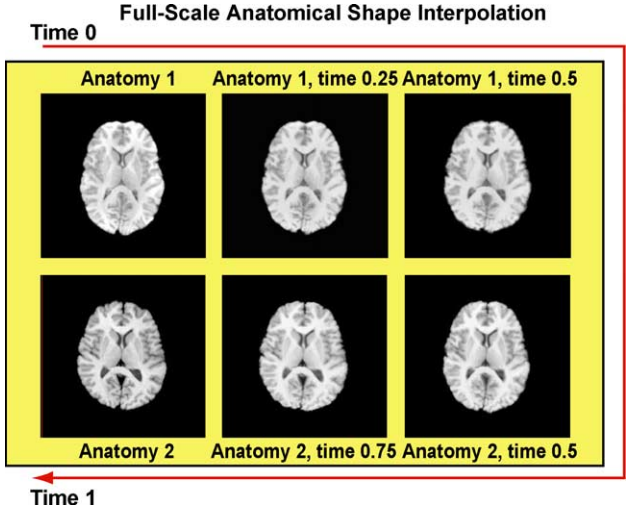


Fig. 11. Three time points of scale consistent shape interpolation are generated from a pair of anatomical instances. The pairwise symmetric registration method used here insures that the interpolated anatomy is consistent for all scales of information. The original images are at top left and bottom left, respectively. This anatomical pair is in correspondence at time 0.5, which is the average of the anatomy at time 0 with the anatomy at time 1. Note that here we have used the topology of the closest anatomy at all points. It would also be natural to use an intensity average where the relative weights are determined by the time values.

(4) Find the new $\bar{\boldsymbol{g}}$ in the domain of the original anatomical estimate through composition, $\bar{\boldsymbol{g}}^{-1,\ t+h}(\boldsymbol{x}_{t=0}) = \bar{\boldsymbol{g}}^{-1,t}(\mathbf{Id} + \bar{\boldsymbol{v}}(\boldsymbol{x}))$.

(5) Repeat until $\bar{\boldsymbol{g}}$ converges and all images are registered.

This algorithm is the mean flow version of the pairwise algorithm and an extended form of $\mathcal{A}$. It is initialized at time zero with a candidate anatomy $\boldsymbol{I}_i$ from the data set, with $\bar{\boldsymbol{g}} = \mathbf{Id}$ and $\bar{\boldsymbol{x}} \approx \bar{\boldsymbol{g}}\mathbf{x_i}$. The anatomy then flows toward the mean configuration giving, ultimately, $\bar{\boldsymbol{g}}^{-1}\bar{\mathrm{x}} = \mathbf{x_i} = \boldsymbol{x}_{\mathbf{t}=0}$. The norms of the velocity $\boldsymbol{v}$ and $\bar{\mathrm{v}}$ at each time are held to a small constant arc length during this algorithm such that $\|\boldsymbol{v}_i\|_L = \|\bar{\boldsymbol{v}}\|_L$. As in the pairwise case, the diffeomorphic framework is used to flow an initial mean shape estimate along a geodesic path toward the centroid of the database as determined by the optimization criterion. The mean flow is estimated with a constant arc length step size giving a strong estimate of the geodesic distance and attempts to convey an equally weighed contribution of each anatomy to the mean. This algorithm outputs the distance from the original image to the mean shape as well as the jacobian of that transformation. Note that registration of each individual image toward the mean $I$ will proceed even if the mean flow stabilizes. An example of this algorithm operating in three dimensions is shown in Fig. 12 while it is illustrated in Fig. 13. Jacobians of the mean flow are shown in Fig. 14.

## Results

We now show an experimental comparison between the two algorithms above, results of which are summarized in Fig. 16. Note that this is an evaluation that only investigates the intensity optimization and does not use anatomical information explicitly. For each of three initial estimates to the mean anatomy, we:

(1) Compute the linear and the geodesic average to the database.
(2) Compute measures of the deformation-based distance and the intensity distance (SSD) to the database by registering all

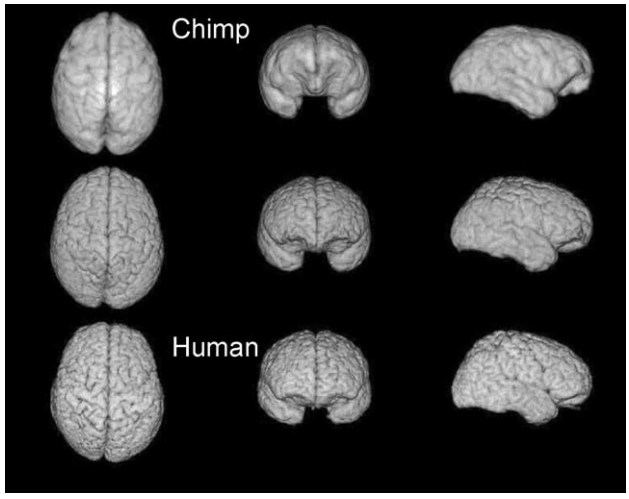


Fig. 12. The top row shows the geodesic anatomical average computed from a database of six chimpanzee cortices. The bottom row shows the same for a database of six human cortices. The middle row shows the anatomical average of all 12 images, where the human was used as an initial estimate. After the registration process converged, the intensities were linearly averaged to produce estimates of a "missing link" (center row) neuroanatomy that is midway between chimp and human in terms of shape and intensity.

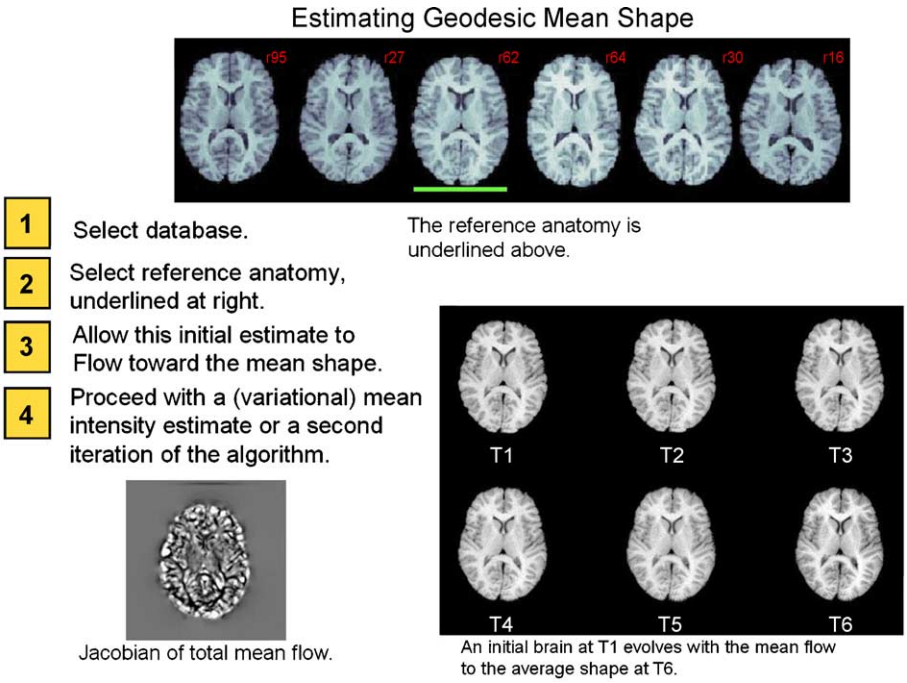


Fig. 13. A sketch of the algorithm for computing the mean geodesic flow.

images to the atlas. Linear averaging is performed on the displacement field output by the large deformation algorithm.

(3) Compare the consistency between atlases constructed from different initial configurations. This involves comparing intensities of the different estimated atlases. The intensities should be very similar if they converge to a very similar solution (as determined by image, not anatomical, information).

This allows us to compare the atlases with respect to the quantities the algorithms minimize. The SSD is measured between the atlas and the original unregistered data set (1st number in each entry in the SSD column) and the atlas and the registered data set (2nd number in each entry in the SSD column). The linear algorithm was iterated until convergence for this study. Inter-atlas consistency measures the SSD between the mean of the atlas intensities and atlases 1, 2, and 3 for each algorithm (Fig. 15).

The geodesic averaging algorithm has several practical advantages over the linear case. As expected, it supplies a more optimized intensity configuration than the linear atlas, as indicated by the numerical data in the SSD column of Fig. 16. The total SSD between the final atlas and the database is measured both before registration (first entry in column) and after registration (second entry in column). Relatedly, the computed atlases are more consistent with respect to the point to which they converge (again, measured through the intensity values), making it less sensitive to the original atlas selected. Iteration of the algorithm is likely to minimize the sensitivity to the initial configuration even further. The geodesic mean also grants a better distribution in the optimization parameter space, as shown in Fig. 18. This may also be seen in the numerical graphs of Figs. 17 and 18. Also, the geodesic average requires less deformation to exhibit better similarity values than with the linear average. The only advantage the linear atlas has is in revealing a configuration that is overall "closer" than accorded by the large deformation atlas. This is the hypothesized result and it is important to note that although proximity is minimized, deformation is not.

Intensity averaging may also be incorporated into these algorithms, as in Davis et al. (2004). However, one must take care that false topologies are not created during this process, which is difficult when using linear intensity averaging. Furthermore, linear averaging may also create intensities that do not appear in

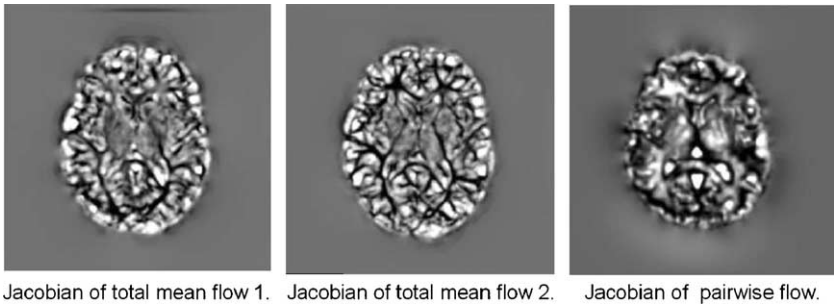


Fig. 14. Comparison of the typical jacobian from two mean flow calculations and one from a pairwise image registration. The mean flow jacobians appear to have more of a "medial" structure than the more diffuse pairwise jacobian.

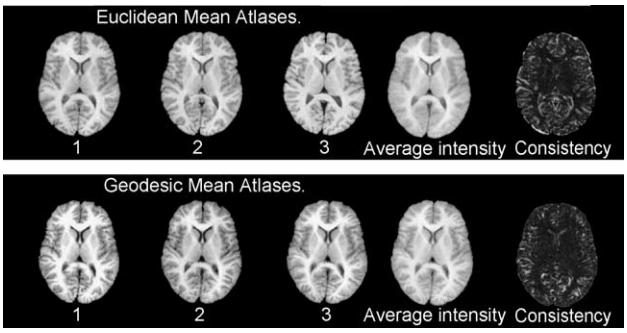


Fig. 15. The images in the top row are the evaluation results of the linear averaging on a database of six human cortical images. The bottom row shows the same for the geodesic averaging. The interatlas intensity consistency is rescaled to show details.

the original data set (consider the case of data with discrete steps in intensity) causing false information to be introduced. Thus, it is important to either insure correct tissue types are aligned or to use a second optimization step for best estimating photometric transformations (Miller and Younes, 2001). Another interesting observation is that jacobians produced by the mean flow have a notably different appearance as can be seen in Fig. 14. The origin of this distinction is still under investigation.

## Conclusion

This paper gave a novel approach for performing geodesic averaging of shape along anatomical image registration manifolds. The design involves transferring algorithmic knowledge about the pairwise registration case into a database-wide registration. The foundational algorithm, here, is an extended version of the viscous fluid framework, but the basic ideas could also be used with other algorithms, such as elastic image registration (Gee and Bajcsy, 1999). Applications of the methods in two and three dimensions were shown and should be useful in future comparative studies of populations with very different topology or large deformations in shape.

Two additional applications of the theory were illustrated. First, an inverse consistent image registration algorithm is conferred by simply integrating velocity fields both forward and backward in time. This allows the images to meet at the mean configuration and the full correspondence to be gained by composition. Second, the theory invites a natural way to find a constant arc length parameterization of the interpolation between two anatomical images. This can be important in both image registration and anatomical modeling (Sundaram et al., 2004).

The algorithm was motivated by the need to couple the image registration and atlas creation process directly in an optimization framework. Results are better than linear averaging as the optimization assumptions of the registration algorithm are maintained by construction. An open question is why the jacobians from the average flow look qualitatively different and if this would have an effect on morphometric calculations. Also, it is not clear what, if anything, this means about the underlying transformation. It is possible that the transformations, originating from time integration of averaged, symmetric flow, tend to focus on the interiors of smooth structures, rather than only at their borders.

Another important contribution of this work is that the framework sets up large deformation statistical analyses. The ability to locally analyze the flows themselves for statistical meaning is useful in modeling and simulating growth and development as well as atrophy and normal shape variation. The locally linear structure of the optimization manifold makes it potentially feasible to use linear statistics such as principal components analysis.

One major weakness in this current work is the lack of anatomically based evaluation and also the small database sizes. The first issue will be addressed by performing landmark or segmentation-based geodesic averaging. The algorithm remains essentially the same as is developed here but with the intensity-based similarity replaced with landmark information. When more efficient three-dimensional implementations are completed, we intend to make the ITK code (Yoo, 2003, 2004) used in this work publicly available and also to study in detail the effect of database size and outliers on the atlasing process. This is a very difficult and open question that will be important to investigate. Future work

| Averaging algorithm | SSD (intensity-$mm^2$) | Curved Distance | Linear distance | Inter-atlas consistency (intensity-$mm^2$) |
|---|---|---|---|---|
| Curved | Better<br>(*) 14.8<br>(**) 2.90 | Better<br>1.12 | 3.05 | Better<br>5.004 |
| Linear | <br>(*) 16.3<br>(**) 3.21 | 1.18 | Better<br>2.90 | 9.079 |

Fig. 16. Table summarizing the numerical results that compare the atlases with respect to the quantities the algorithms minimized. For each algorithm, we compute the sum of squared intensity differences (SSD) and both linear and curved distances. The linear algorithm was iterated until convergence for this study. The SSD is measured between the atlas and the image data set both before (*) and after (**) the data set is registered to the atlas. The curved distance (column 2) is the total of distances defined by Eq. (4). The geodesic atlas has a better SSD when measured from itself to the original database. It also gives a better SSD when measured from itself to the registered database. Interatlas consistency measures the SSD between atlases 1, 2, and 3 for each algorithm.

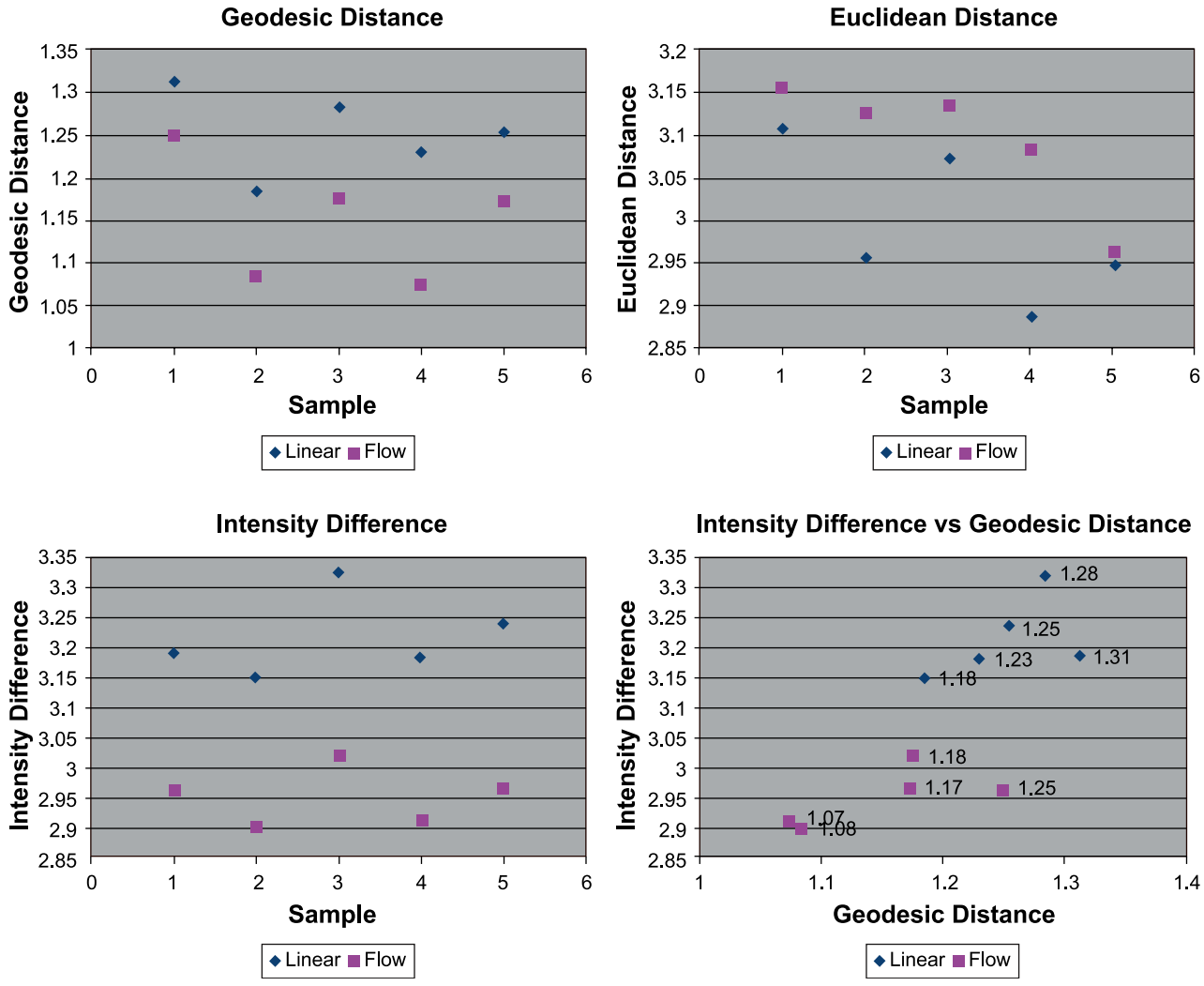


Fig. 17. Graphs summarizing the numerical results.

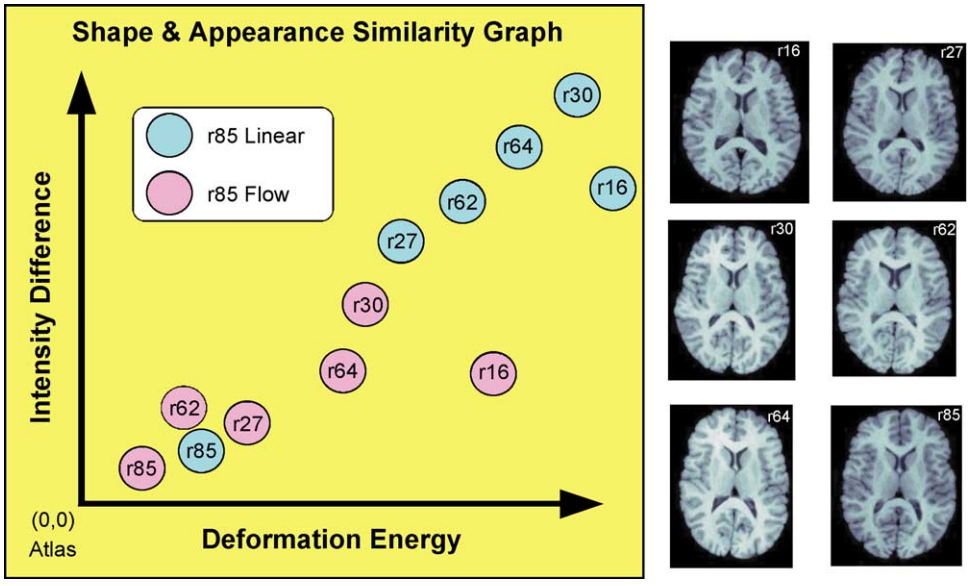


Fig. 18. This graph summarizes the improved distribution of shape and intensity differences when using a geodesically averaged vs. a linear atlas.

will also include further investigation of accommodating large photometric variability through variational and robust methods similar to those contributed here.

## Acknowledgment

The authors would like to acknowledge Tom Schoenemann of the University of Pennsylvania Department of Anthropology for providing data and motivation for this work.

## Appendix A. Transformation inversion

The deformation inversion process is solved as a boundary value problem using a fast nearest neighbor interpolation in the forward direction. An alternative method is in Guimond et al. (2000). The time integrated mean displacement field $\bar{\mathbf{u}}$ is applied to the original positions $\boldsymbol{x}$ of the initial anatomy. The warp is inverted by computing $\bar{\mathbf{u}}^{-1}$ which submits $\bar{\mathbf{x}} + \bar{\mathbf{u}}^{-1} = \boldsymbol{x}$. However, due to the deforming nature of $\bar{\mathbf{u}}$, the definition of $\bar{\mathbf{x}}$ may not be dense. Thus, we use the following algorithm,

(1) Define $\mathbf{p}_i$ as a pixel in the forward domain and *NN* as the nearest neighbor operation.
(2) $\forall \mathbf{p}_i$ with $\mathbf{p}_i = NN(\boldsymbol{x} + \bar{\mathbf{u}})$, fix $\bar{\mathbf{u}}^{-1}(\mathbf{p}_i) = -\bar{\mathbf{u}}$.
(3) $\forall \mathbf{p}_j$ without $\mathbf{p}_j = NN(\boldsymbol{x} + \bar{\mathbf{u}})$, $\bar{\mathbf{u}};^{-1}\, \mathbf{p}_j = G_\sigma \star \bar{\mathbf{u}}^{-1}\mathbf{p}_j$
(4) if the change in $\bar{\mathbf{u}}^{-1}$ is small, then return $\bar{\mathbf{u}}^{-1}$, else go to step 2.

Step 2 involves a fast convolution with Gaussian kernel $G_\sigma$. One may use an explicit optimization process over the whole domain using other interpolations or the finite element method, at the cost of additional computation time.

## References

"Allen Brain Atlas," http://www.brainatlas.org.

Ashburner, J., Friston, K., 1996. Fully three-dimensional nonlinear spatial normalization: a new approach. In: Toga, A.W., Frackowiak, R.S.J., Mazziotta, J.C. (Eds.), 2nd Int. Conf. Functional Mapping of the Hum. Brain vol. 3. p. S111.

Avants, B., Gee, J.C., 2004. Symmetric geodesic shape averaging and shape interpolation. Computer Vision Approaches to Medical Image Analysis (CVAMIA) and Mathematical Methods in Biomedical Image Analysis (MMBIA) Workshop 2004 in conjunction with the 8th European Conference on Computer Vision, Prague, CZ., In press.

Avants, B., Gee, J.C., 2004. Shape averaging with diffeomorphic flows for atlas creation. IEEE Int. Symp. Biomed. Imaging.

Christensen, G.E., Rabbitt, R.D., Miller, M.I., 1993. A deformable neuroanatomy textbook based on viscous fluid mechanics. In: Prince, J.L., Runolfsson, T. (Eds.), 27th Annual Conference on Information and Systems. Johns Hopkins Press, Baltimore, MD, pp. 211–216.

Cootes, T.F., Taylor, C.J., Graham, J., 1995. Active shape models—Their training and application. Comput. Vis. Image Underst. 60, 38–59.

Davis, B., Davies, P., Joshi, S., 2004. Large deformation minimum mean squared error template estimation for computational anatomy. IEEE Int. Symp. Biomed. Imaging.

Dawant, B., Li, R., Cetinkaya, E., Kao, C., Fitzpatrick, J., Konrad, P., 2003. Computerized atlas-guided positioning of deep brain simulators: an feasibility study. In: Gee, J., Maintz, J.B. (Eds.), Workshop on Biomedical Image Registration., Philadelphia, July. Springer-Verlag, Heidelberg, pp. 142–150.

Dupuis, P., Grenander, U., Miller, M.I., 1998. Variational problems on flows of diffeomorphisms for image matching. Q. Appl. Math. 56 (3), 587–600.

Fletcher, T., Joshi, S., Lu, C., Pizer, S., 2003. Gaussian distributions on Lie groups and their application to statistical shape analysis. In: Taylor, C., Noble, J. Inf. Process. Med. Imaging vol. LNCS 2732. Springer-Verlag, Ambleside, UK, pp. 450–462.

Gee, J.C., Bajcsy, R.K., 1999. Elastic matching: continuum mechanical and probabilistic analysis (Chapter 11). In: Toga, A.W. (Ed.), Brain Warping. Academic Press, San Diego, pp. 183–197.

Gee, J.C., Haynor, D.R., 1996. Rapid coarse-to-fine matching using scale-specific priors. In: Hanson, K.M., Loew, M.H. (Eds.), Medical Imaging 1996: Image Processing, SPIE vol. 2710, Bellingham, WA, pp. 416–427.

Grenander, U., Miller, M.I., 1998. Computational anatomy: an emerging discipline. Q. Appl. Math. 56 (4), 617–694.

Guimond, A., Meunier, J., Thirion, J.-P., 2000. Average brain models: a convergence study. Comput. Vis. Image Underst. 77 (2), 192–210.

Hellier, P., Barillot, C., Mmin, E., Prez, P., 2001. Hierarchical estimation of a dense deformation field for 3d robust registration. IEEE Trans. Med. Imaging 20 (5), 388–402.

Johnson, H.J., Christensen, G.E., 2001. Landmark and intensity-based, consistent thin-plate spline image registration. In: Insana, M.F., Leahy, R.M. (Eds.), IPMI. Springer-Verlag, Heidelberg, pp. 339–343.

Kikinis, R., Shenton, M.E., Iosifescu, D.V., McCarley, R.W., Saiviroonporn, P., Hokama, H.H., Robatino, A., Metcalf, D., Wible, C.G., Portas, C.M., Donnino, R.M., Jolesz, F.A., 1996. A digital brain atlas for surgical planning, model-driven segmentation, and teaching. IEEE Trans. Vis. Comp. Graph. 2, 232–241.

Le Briquer, L., Gee, J.C., 1997. Design of a statistical model of brain shape. In: Duncan, J.S., Gindi, G. (Eds.), Information Processing in Medical Imaging. Springer-Verlag, Heidelberg, pp. 477–482.

Letovsky, S., Whitehead, S., Paik, C., Miller, G., Gerber, J., Herskovits, E., Fulton, T., Bryan, N., 1998. A brain image database for structure/function analysis. Am. J. Neuroradiol. 19 (10), 1869–1877.

Mackenzie-Graham, A., Lee, E., Dinov, I.D., Pitiot, A., Hu, G., Bota, M., Ding, Y., Capetillo-Cunlife, L., Crawford, K., Trueng, B., Toga, A.W., 2004. Atlas of the C57BL/6 mouse brain: a multimodal, multidimensional approach. J. Anat. 24, 93–102.

Miller, M.I., Younes, L., 2001. Group actions, homeomorphisms and matching: a general framework. Int. J. Comput. Vis. 41, 61–84.

Miller, M.I., Christensen, G.E., Amit, Y., Grenander, U., 1993. Mathematical textbook of deformable neuroanatomies. Proc. Natl. Acad. Sci. U. S. A. 90 (24), 11944–11948.

Miller, M., Trouve, A., Younes, L., 2002. On the metrics and Euler–Lagrange equations of computational anatomy. Annu. Rev. Biomed. Eng. 4, 375–405.

Rueckert, D., Sonoda, L.I., Hayes, C., Hill, D.L.G., Leach, M.O., Hawkes, D.J., 1999. Nonrigid registration using free-form deformations: application to breast MR images. IEEE Trans. Med. Imaging 18 (8), 712–721.

Sundaram, T., Avants, B., Gee, J.C., 2004. A dynamic model of average lung deformation using area-based reparameterization and shape averaging of lung MR images. Proceedings of Seventh International Conference on Medical Image Computing and Computer-Assisted Intervention (MICCAI), To appear.

Talairach, J., Tournoux, P., 1988. Coplanar Stereotaxic Axis of the Human Brain. Thieme, New York.

Tikhonov, A.N., Arsenin, V.A., 1977. Solutions of Ill-Posed Problems. Winston, Washington, DC.

Yelnik, J., Damier, P., Demeret, S., Gervais, D., Bardinet, E., Bejjani, B.P., Francois, C., Houeto, J.L., Arnule, I., Dormont, D., Galanaud, D., Pidoux, B., Cornu, P., Agid, Y., 2003. Localization of stimulating

electrodes in patients with Parkinson disease by using a three-dimensional atlas—Magnetic resonance imaging coregistration method. J. Neurosurg. 99 (1), 89–99.

Yezzi, A., Soatto, S., 2003. Deformotion: deforming motion, shape average and the joint registration and approximation of structures in images. Int. J. Comput. Vis. 53 (2), 153–167.

Yoo, T., 2003. Insight Into Images: Principles and Practice for Segmentation, Registration and Image Analysis. AK Peters Ltd., Natick, MA.

Yoo, T., 2004. Insight Into Images: Theory for Segmentation, Registration and Image Analysis. AK Peters Ltd., Natick, MA.

Zienkiewicz, O.C., 1971. The Finite Element Method in Engineering Science. McGraw-Hill, New York.